



ELSEVIER

Contents lists available at ScienceDirect

Chemical Engineering Science

journal homepage: www.elsevier.com/locate/ces

On the hydrodynamics of airlift reactors, Part I: Experiments



T. Ziegenhein*, J. Zalucky, R. Rzehak, D. Lucas

Helmholtz-Zentrum Dresden-Rossendorf e.V., 01314 Dresden, Germany

HIGHLIGHTS

- CFD-grade data for model validation.
- Locally resolved measurements in the riser and downcomer.
- Reynolds stresses determined with micro-bubbles.
- Transient behavior of airlift reactors.

ARTICLE INFO

Article history:

Received 6 November 2015

Received in revised form

14 April 2016

Accepted 18 April 2016

Available online 29 April 2016

Keywords:

Dispersed gas-liquid multiphase flow

Airlift reactor

Model validation

Particle tracking velocimetry

Turbulence

Videography

ABSTRACT

It is more and more possible to design bubbly flow reactors with methods of the computational fluid dynamics (CFD). Measurements that can be used for model validation, however, are often missing, especially for complex setups like airlift reactors. Such measurements include locally resolved information about the dispersed and continuous phase, particularly the information about the flow field and interface structures are important. In the present work Reynolds stresses, liquid velocity and gas void fraction profiles as well as bubble size distributions are provided at several positions in the riser and the downcomer in a rectangular airlift reactor for this purpose. In addition, the hydrodynamics inside this airlift reactor are described in detail by the measured values.

© 2016 Elsevier Ltd. All rights reserved.

1. Introduction

Multiphase reactors are used in a wide range of industrial applications. For example, the momentum, heat and mass transport in a fluid is intensified by aerating. As a result, complex flow phenomena arise in simple reactor geometries, from which a bubble column might be the simplest form. Here, the gas bubbles drive the flow and the liquid is rising in the center and falling near the wall in general. The up- and downward flow are next to each other and can interact. Alternatively, internal walls can be placed in bubble columns to separate the up and downward flow; these reactors are called internal airlift reactors.

For many applications that use airlift reactors it is important to know the exact fluid dynamics. For example, the light exposure of microorganisms in airlift photo bioreactors can be optimized by knowing the fluid dynamics (Fernandes, et al., 2010). Moreover, the shear rate and turbulence parameters are important for all process with microorganisms (Liu and Tay, 2002) (Miron, et al., 2000) (Oliver-Salvador, et al., 2013) and for mass transfer

modeling (Korpjarvi, et al., 1999) (Lu, et al., 2000). Nevertheless, such detailed information of the fluid dynamics is rarely accessible by the use of experiments.

A better understanding of the underlying fluid dynamics is gained by using the methods of the computational fluid dynamics (CFD). The Eulerian two-fluid approach is a widely used approach (Ziegenhein, et al., 2015) (Luo and Al-Dahhan, 2011) to model the dispersed multiphase flows that occur in airlift reactors. Using the two fluid model, the multiphase problem is described by phase averaged equations. As a result, the interactions between the dispersed phase and the liquid phase have to be modeled by closure models (Ishii and Hibiki, 2006). Those closure models exist in a large variety; they are often selected to a specific problem dependent on the agreement with an experiment, which is in the end a fitting. However, a reliable set of closure models is necessary to predict unknown setups. Therefore, an extensive model validation is required (Lucas, et al., 2016).

For such a model validation, comprehensive experimental data are needed. Such data have to provide locally resolved flow parameters since all effects in bubbly flows are strongly connected to each other. Moreover, the data should include the gas volume fraction, the liquid velocity, basic turbulence parameters and the

* Corresponding author.

bubble size distribution. In particular, the bubble size distribution is of importance because all closure models depend on the bubble size.

A lot of work was done simulating airlift reactors in the past with the Eulerian two-fluid approach. However, in general the bubble sizes were not known (Huang, et al., 2010) or only known in the downcomer (Luo and Al-Dahhan, 2011). Moreover, often only integral measured values were available (Simcik, 2011) (Ghasemi and Hosseini, 2012). Hence, a validation of the closure models in airlift reactors is limited with the existing experimental data.

The motivation of the present work is to provide a comprehensive set of locally measured data in an internal airlift reactor for the validation of CFD methods. To the best of our knowledge, those measurements were not published in the past and are urgently needed. Moreover, the measured data provide a complete picture of the flow in an internal airlift reactor.

2. Experimental setup

The used rectangular Plexiglas[®] bubble column with internals is shown in Fig. 1. The cross section of the airlift reactor is 0.25×0.05 m. The 5 mm thick internal walls separate the 0.12 m wide riser from the downcomers. Each downcomer has a width of 0.06 m so that the riser and the sum of both downcomers have the same cross section. The distance from the ground plate to the beginning of the internal walls is 0.06 m, which is equal to the width of a downcomer. In addition, the distance from the top of the internal walls to the water surface (the top clearance) is held constant to 0.06 m for all gas volume flows. Thus, the liquid level is at 0.72 m above the ground plate for all setups.

Liquid velocity, turbulent kinetic energy, available Reynolds stress tensor components and bubble sizes are determined at a height of 0.2 m and 0.6 m in the riser and the downcomer, which

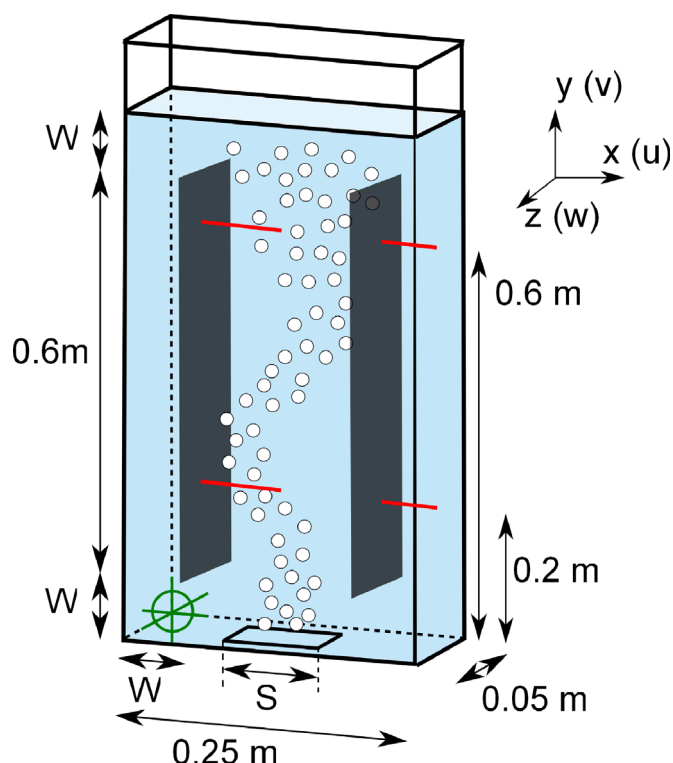


Fig. 1. Experimental setup, lines label the measuring positions. The origin of coordinates is in the bottom left corner.

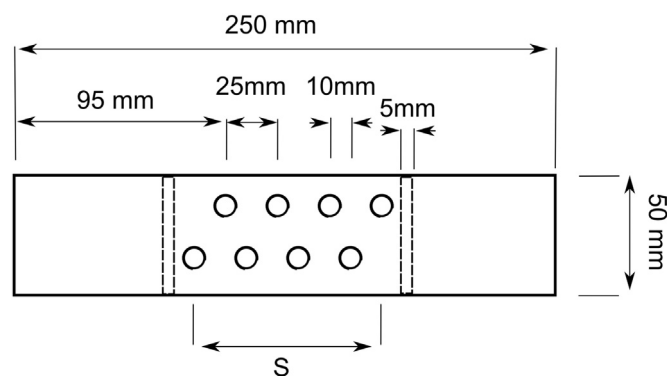


Fig. 2. Ground plate of the airlift reactor.

is indicated with red lines in Fig. 1. The void fraction is measured at a height of 0.6 m in the riser. In addition, the bubble size distribution and the void fraction are determined along the downcomer.

Rubber seals that are attached at the side of the internal walls hold them in place. Therefore, no interaction between the riser and the downcomer is possible and no flow disturbing installations are needed to hold them in place. The gas is injected through the ground plate, which is shown in Fig. 2, by using up to eight needles with an inner diameter of 0.6 mm. The volume flow per needle is held constant for all cases to get a similar bubble size distribution. The total gas volume flow is regulated by changing the needle count. A summary of the important parameters is given in Table 1.

3. Measuring methods

The bubble size distribution is determined with videography at several positions, which is discussed in Section 3.1. The volume fraction in the riser is measured with a conductivity needle probe. In contrast, the volume fraction in the downcomer is determined with videography. Both methods are discussed in Section 3.2. The liquid velocity and the turbulent kinetic energy are measured with particle-tracking velocimetry using micro bubbles (BTV), which is discussed in Section 3.3. All image processing is based on own developed programs.

3.1. Bubble size distribution

The bubble sizes are determined by using digital image analysis. Despite a certain amount of automation, e.g. as discussed by Broeder and Sommerfeld (2007), bubble sizes have to be identified by hand in complex flow situations, which occur in the riser for all cases as illustrated in Fig. 3. Edge detecting algorithms are used to speed up the manual bubble identification, so a large amount of bubbles can be tracked. Nevertheless, as bubble clusters occur in all complex flows, bubbles are overlaid by other bubbles, which lead to problems. The structure of the cluster, however, is changing

Table 1
Experimental parameters at standard conditions.

Case number	Volume flow (l/min)	Sparger needle (mm)	Needle count	Volume flow per needle (l/min)	S (mm)	W (gas on) (mm)
4	3	0.6	4	0.75	35	60
6	4.5	0.6	6	0.75	60	60
8	6	0.6	8	0.75	85	60

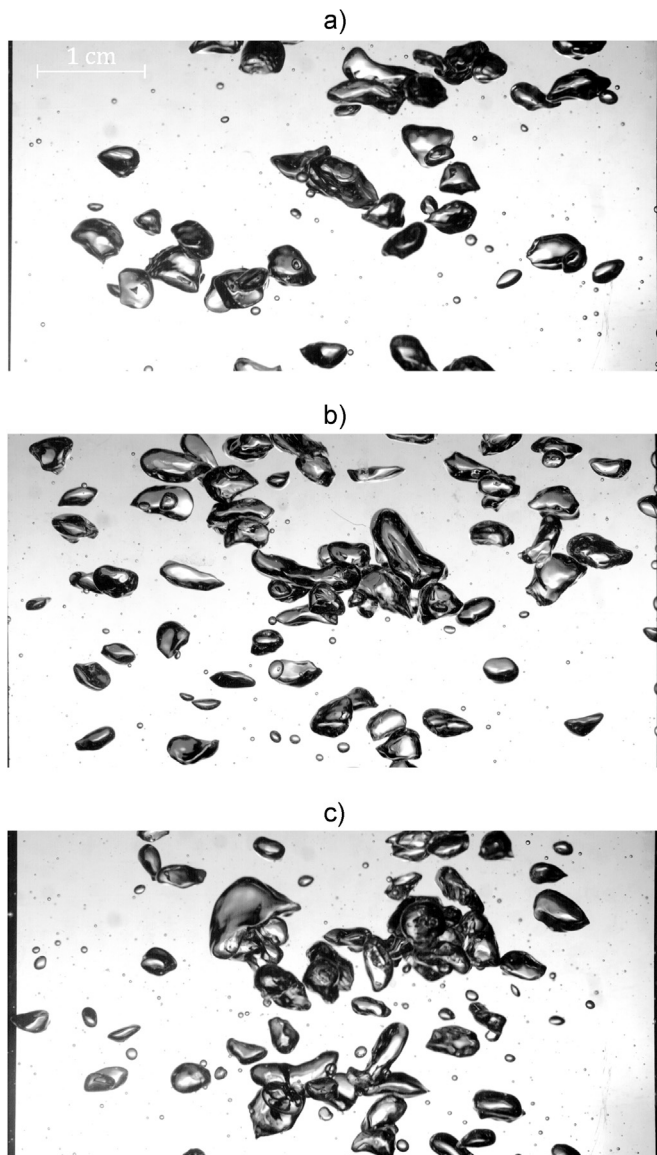


Fig. 3. Bubble size distribution in the riser at a height of $y = 0.2$ m. (a) Case 4, (b) case 6, and (c) case 8.

over time; therefore, several photographs are taken and the background bubbles are evaluated when they are seen clearly.

This procedure is demonstrated in Fig. 4. A bubble cluster is observed over ten frames and the viewable bubbles are determined in Frame 0, Frame 5 and Frame 10. However, not all bubbles could be evaluated because the bubble in the upper left corner is behind the other bubbles all the time. This error appeared seldom in the evaluation and might be negligible. The averaged spherical equivalent diameter of the solid of revolution of the projected area is determined by evaluating 2500 bubbles per measurement. Bubbles that are smaller than 1.5 mm are not evaluated in order to reduce the measuring effort since the count of the small bubbles is large, whereas such small bubbles are not significant for the Sauter diameter as shown in the result section.

Compared to the riser, the bubbles and the void fraction in the downcomer are smaller so that the bubble size distribution is determined fully automated. Nevertheless, bubbles overlay other bubbles, too. Hence, the treatment of the overlaid bubbles has to be clarified.

Identifying bubbles that are overlaid by other bubbles is simple, but identifying whether a bubble is in front or not is more difficult

(Honkanen, et al., 2005). In addition, the reconstruction of the bubble(s) in the back is challenging (Broeder and Sommerfeld, 2007). Until now, no reliable and/or efficient methods exist for this purpose. Thus, only the non-overlaid bubbles are used to determine the bubble size distribution.

Determining the bubble size distribution from the non-overlaid bubbles only, imposes the assumption that all bubbles have the same probability to be overlaid; else, a wrong result would be obtained. This assumption is only appropriate if the bubble size distribution is narrow. Consequently, using this method the worst results are expected for case 8 because for the highest gas volume flow-rate the highest volume fraction and the broadest bubble size distribution is expected. For this case, the automatically determined bubble sizes are compared to manual picked bubbles by the use of the method described above. As a result, the automatically determined values are underestimated by 5%. Consequently, the bigger bubbles have a higher probability to be overlaid by other bubbles, which is consistent to the findings of Kracht et al. (2013).

The algorithm for the automated determination is demonstrated in Fig. 5. At first, the raw picture is segmented by the use of an adaptive threshold to divide the black surrounding of the bubble and the translucent inside. Afterwards, the bubbles are identified by a simple divide and conquer algorithm.

Parallel, the boundary of the bubbles and the bubble clusters are determined with an edge detecting algorithm (Canny, 1986), which is demonstrated in Fig. 5c. The detected boundaries are combined with the result of the segmentation; if inside a boundary more than two bubbles are found, the area inside the boundary is treated as overlaid bubbles. Finally, the non-overlaid bubbles are used for the evaluation.

The error of the segmentation is negligible; it was found that 3 of 1000 bubbles are not identified by the algorithm. The smallest bubble size was chosen to be 1.5 mm, which is consistent to the smallest evaluated bubble size in the riser. To determine the bubble sizes in the downcomer, 5000 pictures were recorded every 0.5 s per case; with this procedure around 300,000 bubbles were evaluated per case.

3.2. Volume fraction

The volume fraction in the riser is measured with a conductivity needle probe. The performance of the needle probe is discussed in several studies, e.g. by Le Corre et al. (2003), or by Manera et al. (2009). In the present work, a single needle probe is used, which has been described by Da Silva et al. (2007) and Schleicher et al. (2008). The 0.2 mm diameter probe lance is assembled movable at the top of the airlift reactor.

A needle probe, however, is not usable in the downcomer because the bubbles have a very small absolute velocity. Moreover, the probe would significantly disturb the flow in the narrow channels of the downcomer. Thus, the void fraction in the downcomer is determined with photometric methods by multiplying the bubble count with the averaged bubble volume divided by the measuring volume.

For this purpose, the method for the bubble size measurement given in Section 3.1 and shown in Fig. 5 is used. The divide and conquer algorithm, which identify the bubbles from the segmented pictures, gives the count of all bubbles including the overlaid bubbles. From the non-overlaid bubbles, the average volume of the rotated projected area is calculated. This volume is assumed representative for the bubbly flow. Performing this method in different areas of the downcomer the two-dimensional void fraction distribution along the downcomer is obtained. This void fraction is a volume averaged value over the depth of the downcomer, which is recorded by the camera completely.

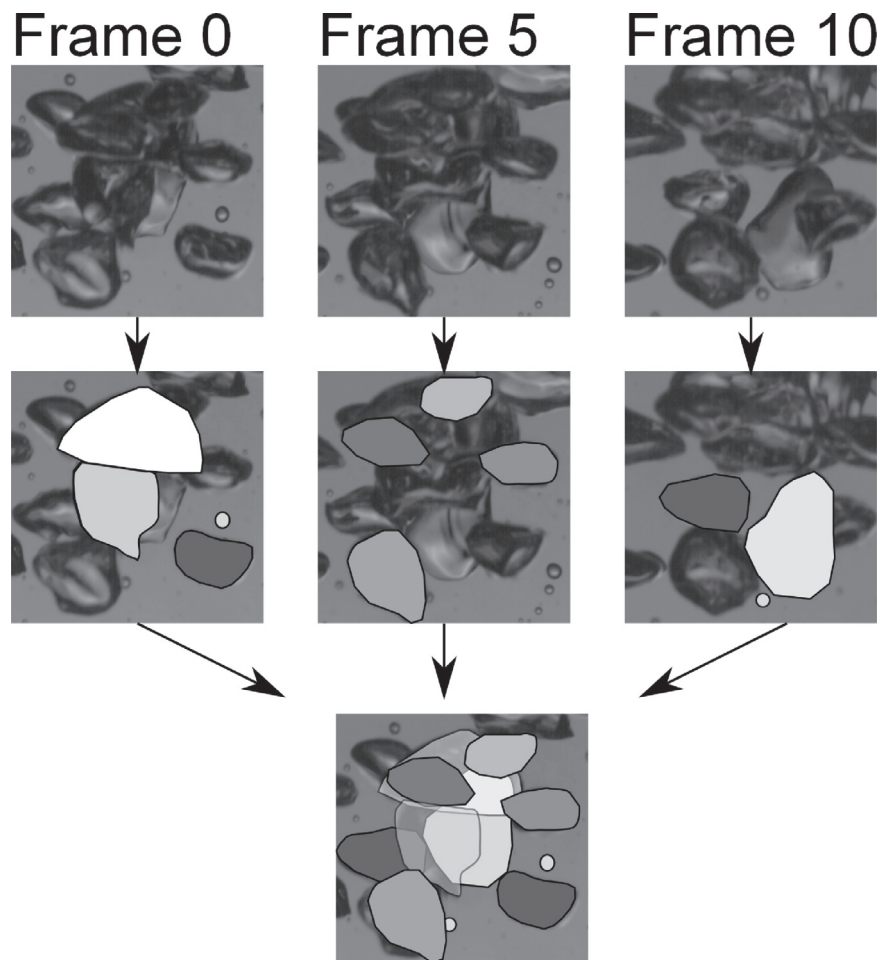


Fig. 4. Determination of the bubble sizes in bubble clusters by observing the cluster over 10 frames with 200 frames/s recording speed.

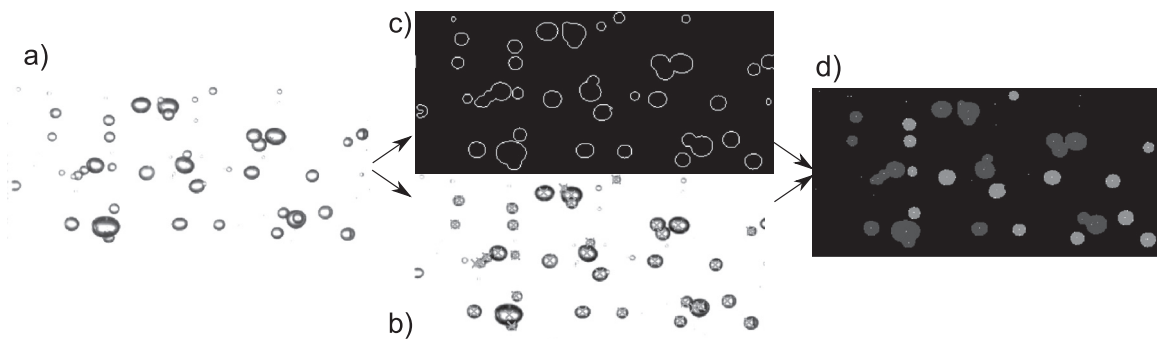


Fig. 5. Automated bubble size determination with detection of overlaid bubbles. (a) Input with corrected contrast (b) segmented bubbles with positions (gray crosses) (c) edge detection algorithm (d) cutting out the overlaid bubbles (dark gray). Only bubbles larger than 1.5 mm are treated.

Using the above-described manual bubble-picking algorithm, the results of the automated void fraction algorithm are compared to an extensive evaluation by hand. As a result, an underestimation of 15% was found for case 8 in the upper region of the downcomer. This error is due to an under prediction of the large bubbles since they have a higher probability to be overlaid by smaller bubbles, which leads to a smaller determined averaged bubble volume. However, for a lower void fraction and a narrower bubble size distribution, e.g. in the lower part of the downcomer for case 8 or for case 4 and case 6 in general, the error is expected smaller.

3.3. Liquid velocity and turbulent kinetic energy

For measuring the liquid velocities, a particle tracking velocimetry method that uses the naturally occurring micro bubbles is used. This bubble tracking velocimetry (BTV) in bubble columns is described recently by Ziegenhein et al. (under review) As no seeding particles that tend to accumulate at the bubble surface are needed, the used purified water truly stays purified during the experiments.

The method is described by Ziegenhein et al. (under review) in detail, including a volume illumination technique, which is also used here. A volume illumination is used in order that higher void

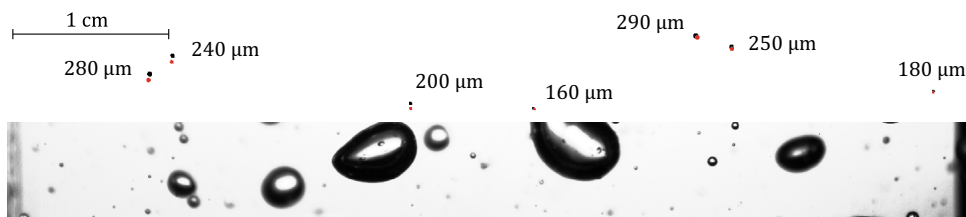


Fig. 6. Bubble tracking velocimetry (BTV) in the downcomer at $y = 0.6$ m for case 6. Below the original image. Above the micro bubble tracks labeled with the sizes of the micro bubbles; the black colored bubbles are in the first recorded image, the red colored bubbles in the last recorded image. The micro bubbles in the above image are enlarged for a better visibility. (For interpretation of the references to color in this figure legend, the reader is referred to the web version of this article.)

fractions can be realized and the internal walls do not disturb a possible light sheet generated from the side. Nevertheless, to get a narrow quasi two-dimensional measuring volume the micro bubbles used for BTV have to be selected in that, which is realized with a 2 mm depth of field of the camera setup. The sharp micro bubbles are picked with an edge filter, which is in detail described in the above-mentioned work. For all liquid velocity measurements, the quasi two-dimensional measuring plane is in the center of the column.

The method is demonstrated in Fig. 6 for case 6 in the downcomer's top region. As can be seen, many blurred micro bubbles are present; these are identified and not taken for tracking. Moreover, the micro bubble sizes are in the range of 160–290 μm , which represents almost the total used range of 150–300 μm . This range was determined previously in bubble columns in similar flow conditions (Ziegenhein et al. in preparation). The rising velocity of the micro bubbles, which is calculated from the drag law of Bozzano and Dente, (2001) has to be subtracted from the measured velocity.

A sampling bias occurs if a not representative sample, in which some values are less likely included than others, is picked (Ziegenhein and Lucas 2016). If the liquid velocity is measured with BTV in bubble flows, such a non-representative sample is picked. Bubbles that are passing the field of view hinder the view on the measuring plane. However, these large bubbles drive the flow so that higher velocities occur just when many of these bubbles are in the field of view. Since these velocities are less likely measured due to the large bubbles in the field of view, a sampling bias occurs. It should be noted, that the sampling bias is not caused by the bubbles inside the measuring plane, but by the bubbles out of it.

The sampling bias is demonstrated in Fig. 7. Clearly, the velocity is correlated to the count of trajectories; if the velocity is high, the count of trajectories is low and vice versa. The graphs in Fig. 7 are moving averaged over four seconds to demonstrate the sampling bias clearly.

A window ensemble average in space and time is used in order to overcome the sampling bias, which is explained in detail by Ziegenhein and Lucas (2016). The window ensemble averaging in

space is executed by dividing the measuring area in grid cells. For window averaging in time, the time is waited until all grid cells contain at least one velocity track. After this time, all velocities that are collected in one grid cell are averaged; this is done for all grid cells. Thus, one value in each grid cell is obtained afterwards. After the complete measuring time, these averaged values are arithmetic averaged per grid cell. The points in the later shown liquid velocity plots are in the center of such a grid cell.

A burst of four pictures is recorded with a frequency of 1600 Hz. The pictures have a height of 7 mm and a length of 70 mm with a resolution of 128×1280 pixel. The micro bubbles are connected to a track by simply determining the nearest particle in the next picture. The velocity is calculated when the bubbles move its own radius, else, the position in the next picture of the four pictures is used. If a bubble does not move its own radius during the four recorded pictures, the first and the last picture is taken for tracking. The bursts are recorded with a frequency of 100 Hz.

The liquid velocity profiles in the riser are obtained from four single measurements with a distinct time between them. In total, 48,000 bursts, which is equivalent to eight minutes measuring time, are evaluated in the riser at a height of 0.2 and 0.6 m. In the upper part of the downcomer at a height of 0.6 m 36,000 bursts are recorded and in the lower part 24,000 bursts. The long measuring time in the riser is necessary because a bubble plume with a very long time scale occurs; especially in the lower part of the riser, this effect is significant.

4. Results

4.1. Bubble size distribution

The bubble size distributions in the riser for the different volume flows are shown in Fig. 8. The bubble sizes are determined at a height of 0.2 m and 0.6 m to evaluate possible break-up and coalescence effects. The number density function is identical at both heights for case 6 and case 4 (case 4 is not shown) so that no coalescence and break up effects occur in the riser. For case 8, the

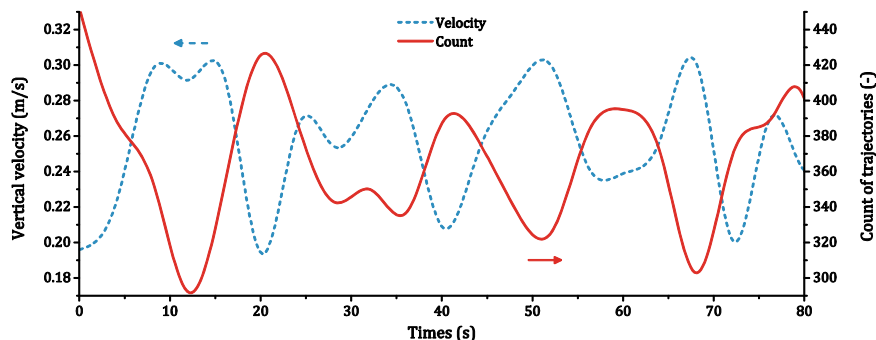


Fig. 7. Sampling bias in the center of the riser at $y = 0.2$ m for case 8. The graphs are moving averaged over 4 s.

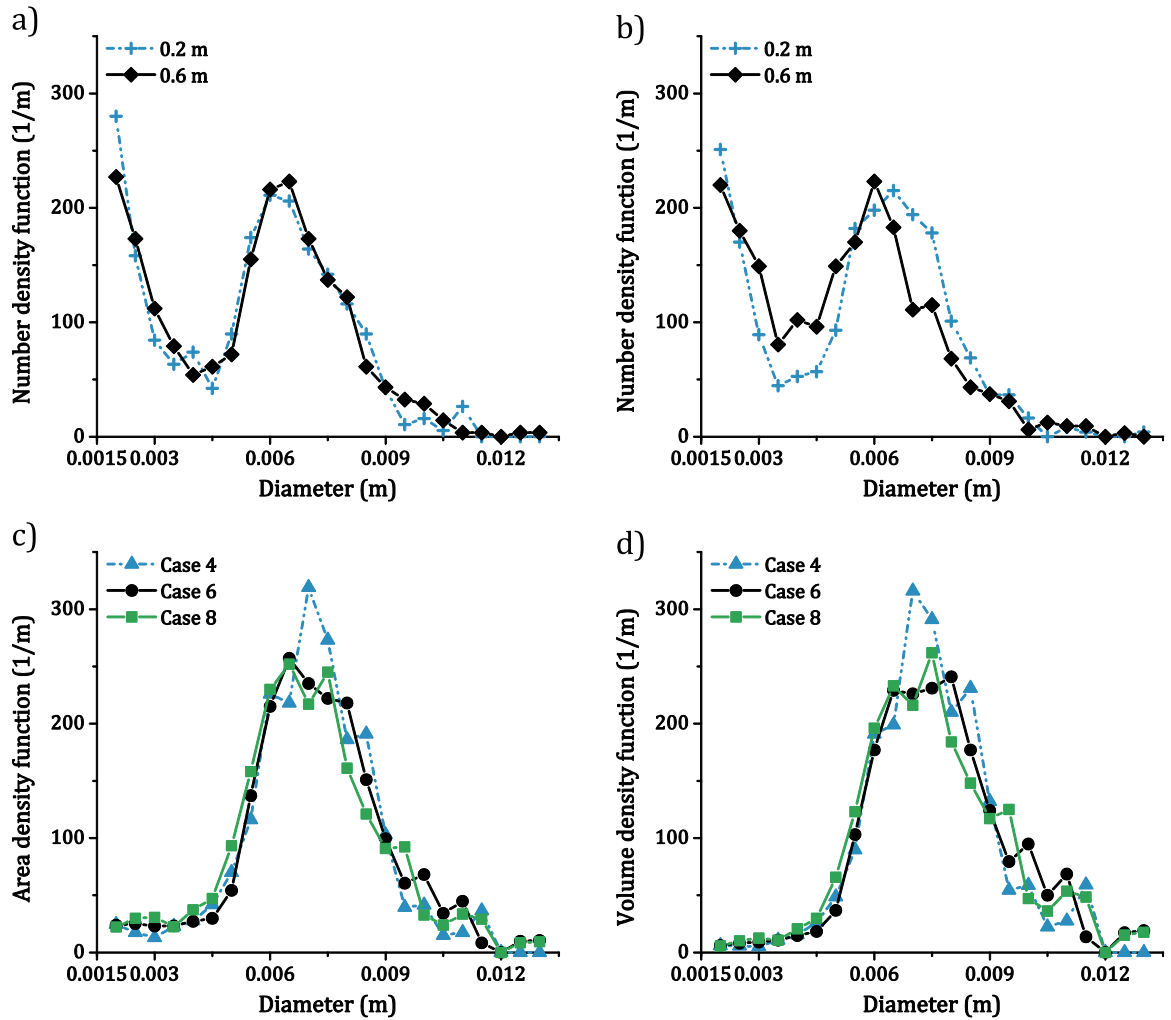


Fig. 8. Bubble size distributions in the riser. (a) Number density for case 6 at two different heights (b) Number density for case 8 at two different heights (c) averaged area density function at 0.2 m and 0.6 m (d) averaged volume density function at 0.2 m and 0.6 m.

number density function is shifted slightly towards smaller bubbles. Nevertheless, comparing the area density and volume density function of case 8 with the results of case 6 and case 4 no large differences are seen so that for all cases the same bubble size

distribution can be assumed.

The automatically determined bubble sizes along the downcomer are shown in Fig. 9a. The bubble sizes are averaged over the cross section of the downcomer. The bubble size at the top of the

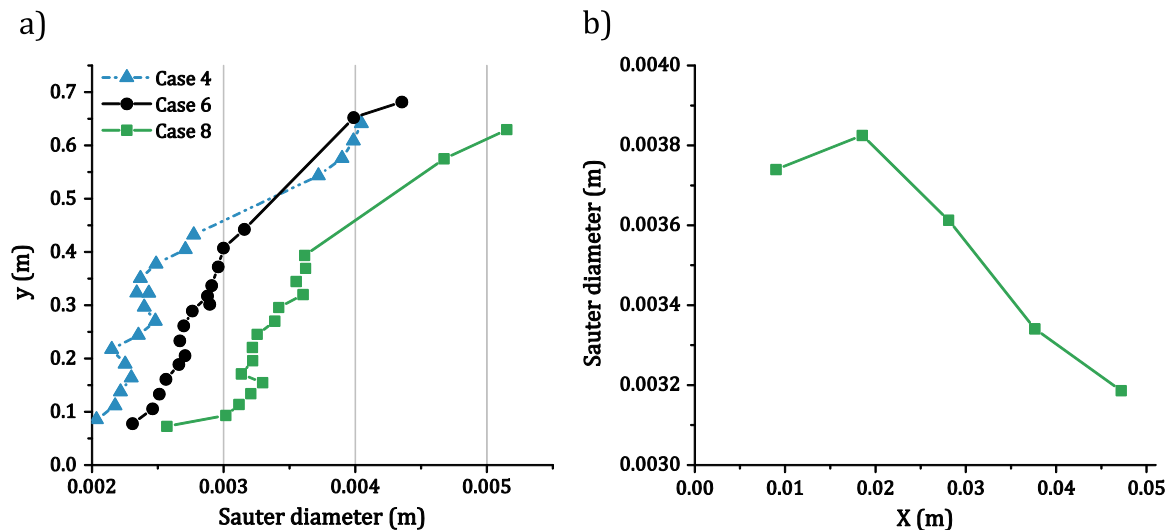


Fig. 9. Bubble sizes in the downcomer. (a) Bubble sizes along the downcomer. (b) Bubble sizes over the width of the downcomer for case 8 averaged over height from $y = 0.3$ m to $y = 0.4$ m.

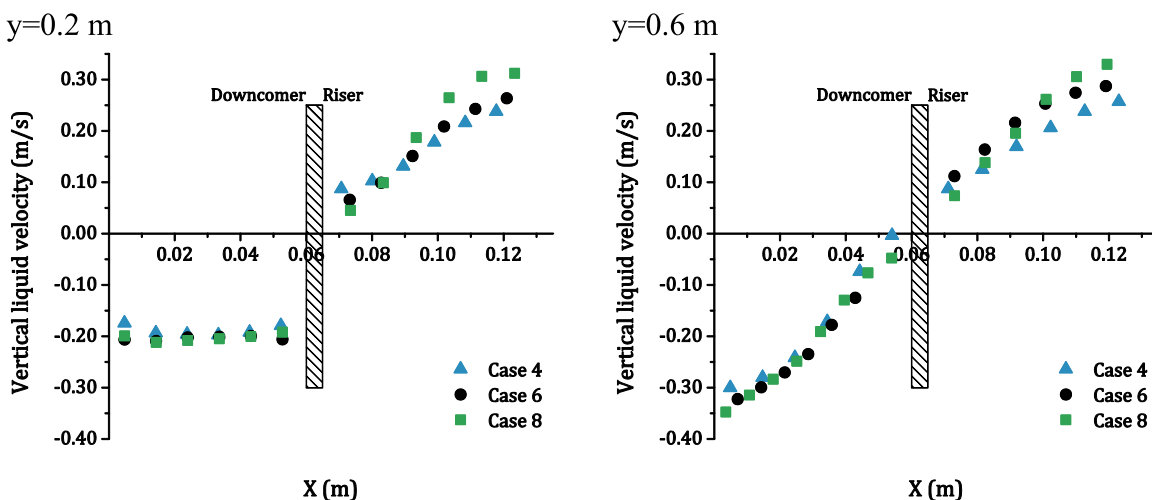


Fig. 10. Liquid velocity profiles measured at two different heights.

downcomer for case 6 and case 8 are determined by hand because the void fraction is too high for an automated evaluation. As can be seen from Fig. 9 a separation of the bubble sizes along the downcomer occurs.

Besides a separation over the height, also a separation of the bubble sizes over the width of the downcomer is seen, as demonstrated in Fig. 9b for case 8. The bubble sizes are averaged over height from $y=0.3$ m to $y=0.4$ m and are plotted against the horizontal coordinate from the airlift reactor wall at $x=0$ m to the internal wall at $x=0.06$ m. Clearly, near the reactor wall larger bubbles are situated compared to the bubbles that are found near the internal walls. This separation is related to the flow structure as will be discussed below.

4.2. Liquid velocity and turbulence

The liquid velocities at two different heights in the riser and the downcomer for the investigated volume flows are shown in Fig. 10. The downcomer is situated from the reactor wall at $x=0$ m to the internal walls at $x=0.06$ m. At a height of 0.2 m, the velocity profiles in the downcomer are flat and are nearly the same for all three flow rates. Surprisingly, the integral averaged velocity for case 6 and case 8 along this measuring line are both almost exactly -0.2 m/s; furthermore, this is nearly the exact value obtained for both cases at the height of 0.6 m in the downcomer. For case 4 a slightly lower averaged velocity of -0.18 m/s at $y=0.2$ m and $y=0.6$ m is obtained.

The qualitatively similar results obtained in the riser at $y=0.2$ m for all cases are due to a distinct bubble plume created by the circulating liquid that constricts the bubbles developed at the

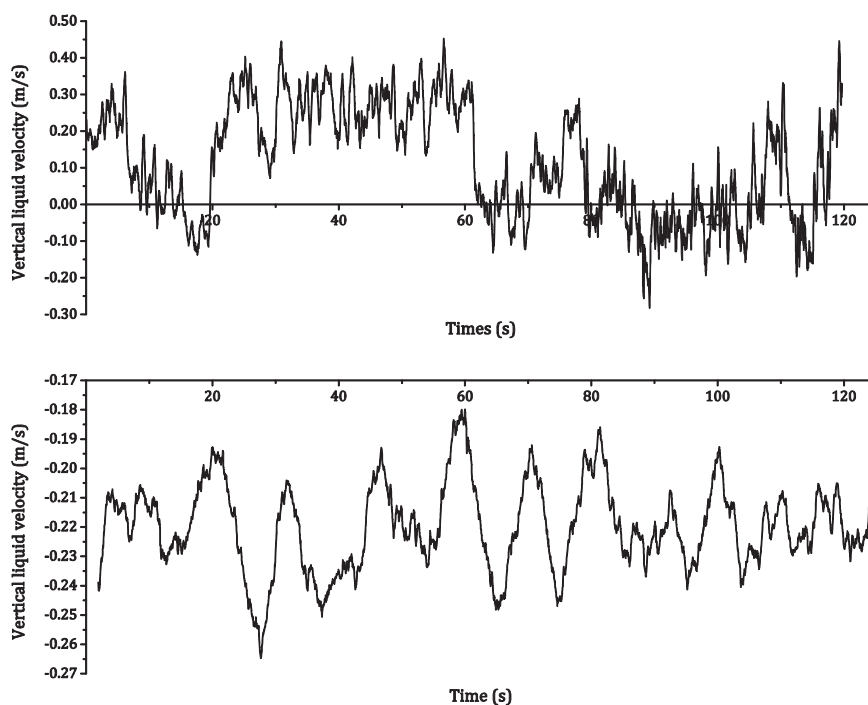


Fig. 11. Vertical velocity over time at two different positions for case 6, the time scale is arbitrary set to zero for both and is not synchronized. Top: the vertical velocity over time in the left quarter of the riser at $x=0.095$ m and $y=0.2$ m; every measuring point is moving averaged over 0.08 s. Bottom: the vertical velocity over time in the center of the left downcomer at $x=0.03$ m and $y=0.6$ m; every measuring point is moving averaged over 2 s.

sparger. In addition, this bubble plume swings from one side to the other. An occasionally asymmetric stabilization at the internal walls of the bubble plume was observed.

The transient liquid velocity results in Fig. 11 demonstrate the occasionally stabilization of the bubble plume at one side. From the transient results in the riser at a height $y=0.2$ m in the left quarter at $x=0.09$ m (upper plot), it is seen that the bubble plume is standing 40 s at the left wall before going to the right wall. However, between 60 s and 110 s a steady bubble plume swinging motion is not seen as well. Nevertheless, a steady swinging motion was dominant during the experiments. This motion is observed in all areas of the reactor as demonstrated in the lower transient vertical velocity plot, which was recorded in the downcomer, in Fig. 11. Here, a more or less steady frequency over 120 s is observed.

The behavior of a standing bubble plume at one side of the riser for a distinct quantity of time was observed for every case. The time that the bubble plume stood at one side seemed to be arbitrary in the range of several seconds to minutes. In addition, the switching between the situations of a permanently swinging motion to a standing one at one wall seemed to be arbitrary. Larger deviations between the four consecutively conducted liquid velocity measurements, as discussed in the method section, were observed, particularly, in the bottom part of the riser.

A more continuous situation is obtained in the upper part of the

the column. The bubble plume is spreading towards the top; also, the results that are obtained from the single measurements are not deviating much. The same is found in the downcomer.

Noteworthy, the vertical liquid velocity in the downcomer at a height of $y=0.6$ m is zero near the internal walls and distinctly negative towards the reactor walls. Consequently, a large standing vortex in this region is observed; the liquid in the top clearance is forced to the side because of the driving force of the bubbles in the riser. Reaching the reactor wall the liquid is pulled downward in the downcomer. From visual observations, bubbles are dragged in the downcomer by the same mechanism. However, many bubbles that are pulled in the downcomer at the reactor walls migrate to the internal walls and rise up at them because of a lower vertical liquid velocity there. This lower vertical liquid velocity at the internal walls was observed along the complete downcomer and can be still observed at $y=0.2$ m for all volume flows.

Despite the averaged liquid velocities being similar for all investigated cases, the normal components of the Reynolds stress tensor $u'u'$ and $v'v'$ shown in Fig. 12 are very different among the volume flows. In general, an increasing of $u'u'$ and $v'v'$ with increasing gas volume flow rate is seen. Looking at the bottom of the riser at a height of $y=0.2$ m, the $v'v'$ graphs show clear maxima located beside the center for all cases. These maxima beside the center are consistent with previous measurements in the bubble plume regime (Ziegenhein, et al. 2016) (Simiano, et al., 2006)

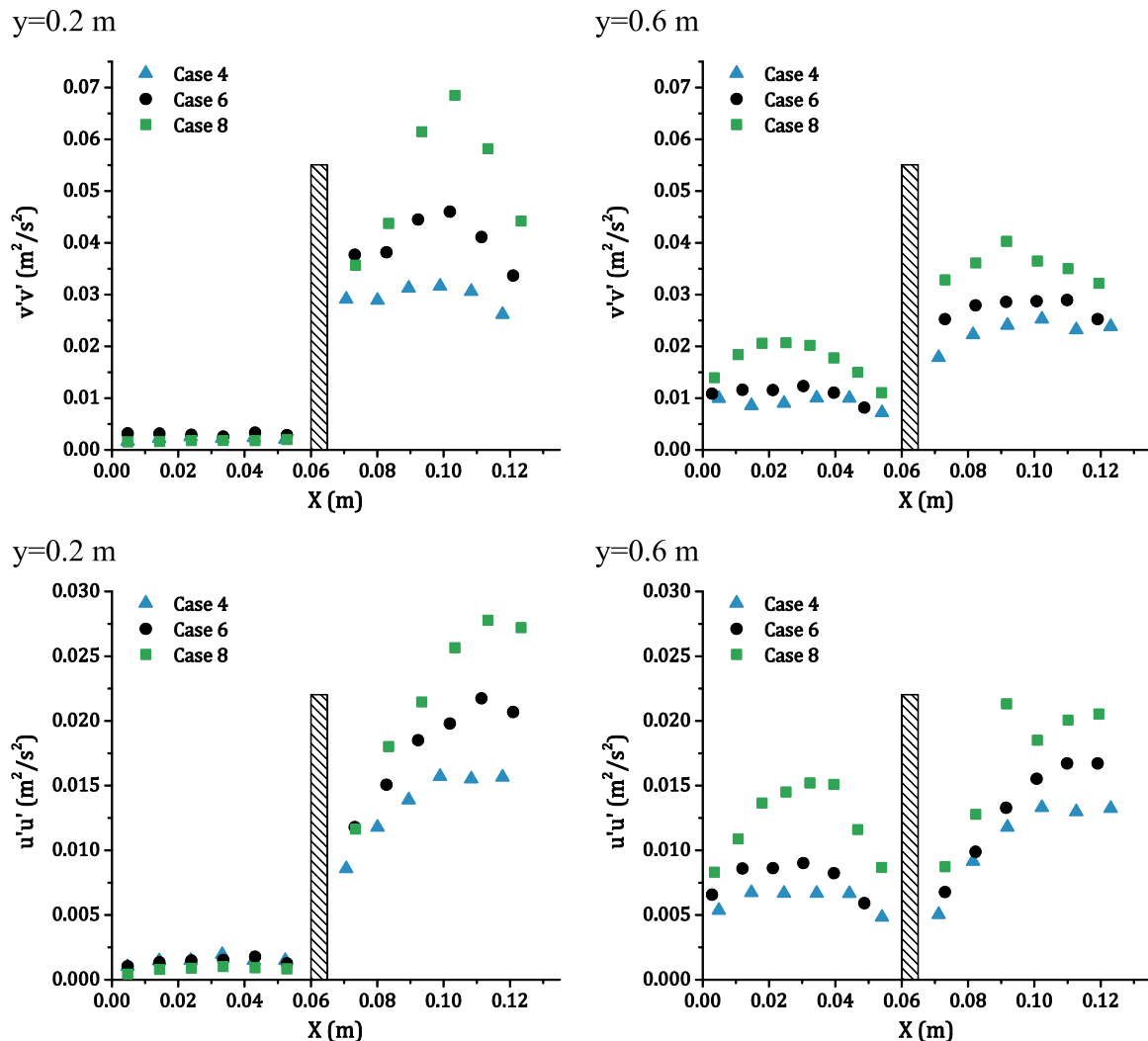


Fig. 12. Normal Reynolds stresses in the vertical ($v'v'$) and horizontal ($u'u'$) direction at two different heights.

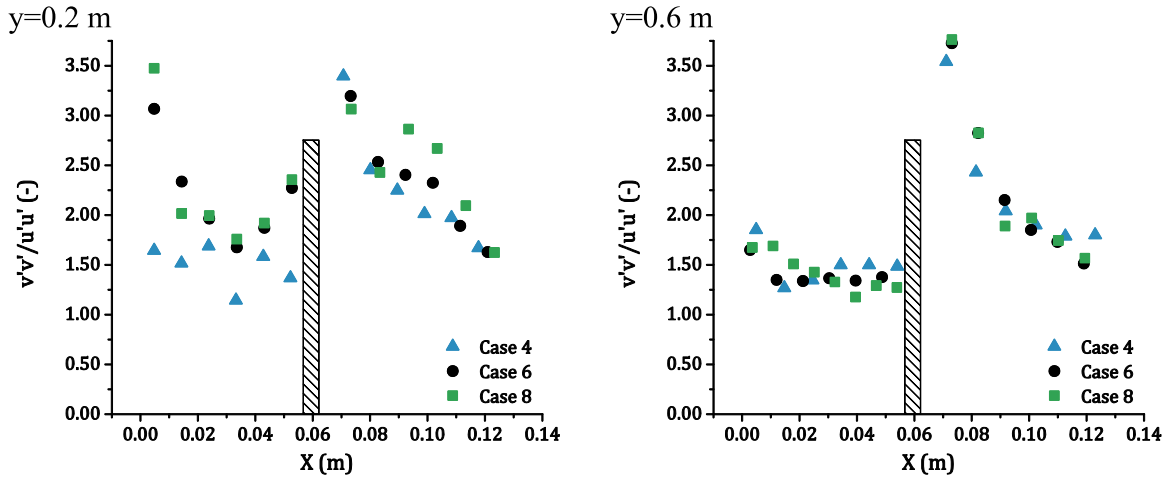


Fig. 13. The ratio between $v'v'$ and $u'u'$ in the reactor.

(Mudde, et al., 1997). In contrast, the $u'u'$ graphs show maxima in the center, which is also observed in the previously mentioned work.

Averaged over the cross section of the riser at $y=0.2$ m, the $v'v'$ values are for all cases nearly twice as high as the $u'u'$ values. The averaged normal components of the Reynolds stress tensor along the centerline seem to increase linearly with the volume flow, for example $0.01 \text{ m}^2/\text{s}^2$ for $v'v'$ from case 4 to case 6 and $0.011 \text{ m}^2/\text{s}^2$ from case 6 to case 8.

With increasing height both $u'u'$ and $v'v'$ are decreasing in the riser as shown in Fig. 12, but the averaged $v'v'$ values remain nearly twice as high as the $u'u'$ values. Looking at the results obtained for case 8 distinct maxima are seen in the $u'u'$ and $v'v'$ graphs at $x=0.095$ m. These maxima can be found in every measurement and are, therefore, no outlier. The origin of this effect is unknown.

Along the downcomer, $u'u'$ and $v'v'$ are decreasing. Moreover, compared to the riser the values in the downcomer are low. Looking at the results in the downcomer at a height of $y=0.6$ m, the obtained profiles for case 4 and case 6 are, surprisingly, similar whereas for case 8 the values are distinctly higher.

The ratio between $v'v'$ and $u'u'$ is shown in Fig. 13. The ratios are very similar for all volume flows, except of case 4 in the downcomer at $y=0.2$ m. In contrast to case 6 and 8 almost no bubbles are found for case 4 at this position, as discussed later on. Interestingly, in the riser at the internal walls $v'v'$ is distinctly higher than $u'u'$. This is also found in the lower part of the downcomer at

the outer wall for case 6 and 8 as well as to a lesser extent in the top part of the downcomer, whereas at the internal walls the ratio is more or less similar as in the center. In the riser at $y=0.2$ m the increasing peak strength of $v'v'$ can be observed very well at $x=0.08$ m. Overall, the ratio is smallest at the top of the downcomer, for all gas volume flows. Since the bubble sizes are very similar for all volume flows it can be concluded that the gas volume fraction do not influence the ratio of $v'v'$ and $u'u'$ except of the peak in the $v'v'$ profile in the plume region at $y=0.2$ m, which is quite surprising.

The relation of increasing turbulent kinetic energy with increasing gas volume flow is shown in Fig. 14. Due to the meandering bubble plume it is expected that the normal Reynolds stress component $w'w'$, w is the not measured liquid velocity component normal to the measuring plane, is small compared to the other two components, $u'u'$ and $v'v'$, so that the turbulent kinetic energy is approximated by the sum of these two. The superficial velocity is based on the cross section of the riser. The ratio of the root mean square of the turbulent kinetic energy and the superficial velocity is decreasing with increasing gas volume flow in all parts of the reactor, which is opposite to the trend of the other investigated quantities. In consequence, the smallest gas volume flow is the most efficient way to generate turbulent kinetic energy in all parts of the reactor, which is important since the gas volume flow is related to pressure work done by pumps.

The cross component of the Reynolds stress tensor $u'v'$ is shown

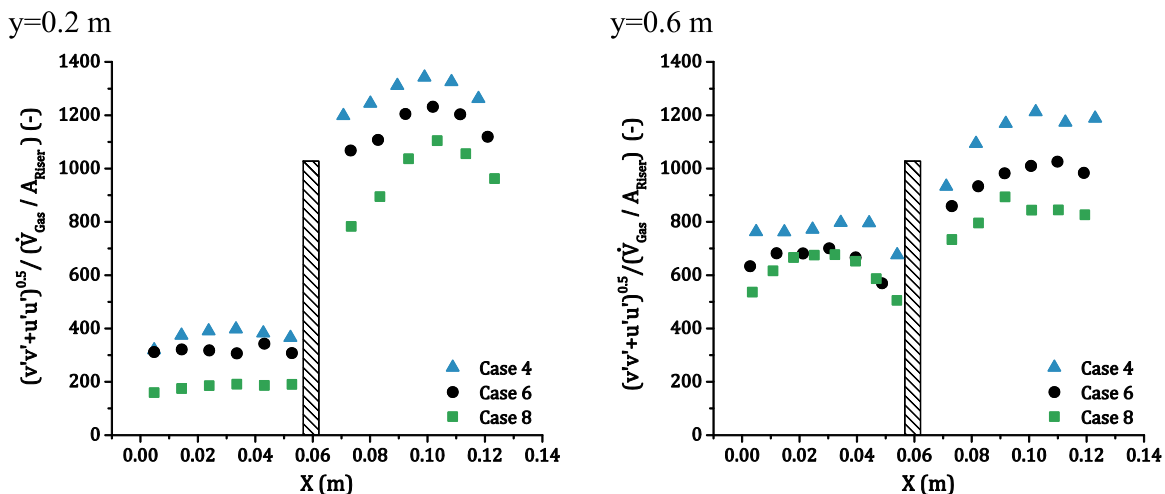


Fig. 14. The ratio of the square root of the estimated turbulent kinetic energy and the superficial velocity with respect to the cross section of the riser.

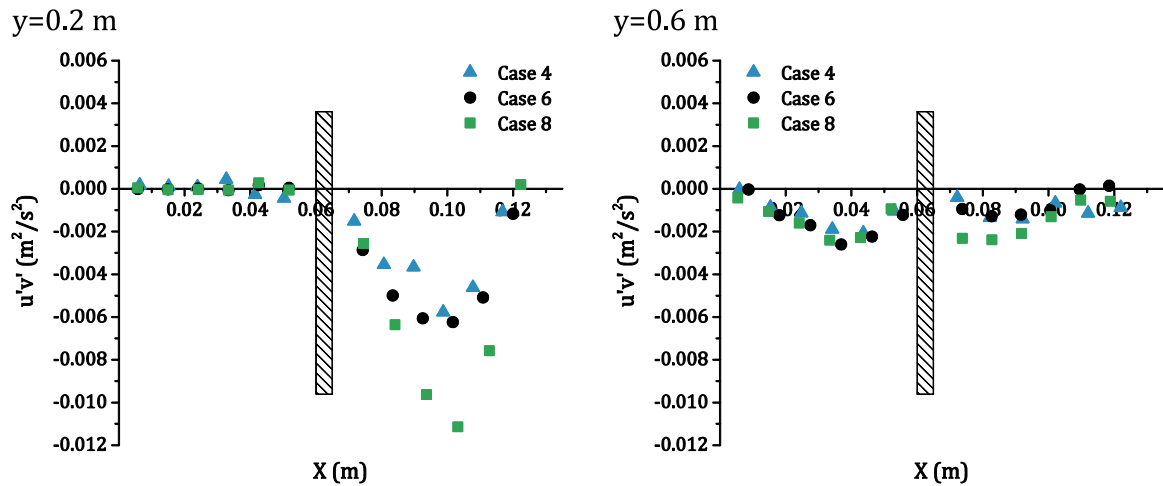


Fig. 15. Cross Reynolds stress d_{BC} at two different heights.

in Fig. 15. Similar to the normal components, large values are obtained at a height of $y=0.2$ m in the riser that are decreasing with increasing height. Although the $u'v'$ values are similar for case 4 and case 6 at $y=0.2$ m in the riser, the values for case 8 are distinctly larger.

In the downcomer at $y=0.6$ m, $u'v'$ is very similar for all cases. Like the normal components, the $u'v'$ values are decreasing along the downcomer to very small values.

4.3. Void fraction

The void fraction was determined inside the riser with a needle probe and along the downcomer by using videography. The void fraction that is measured with a needle probe is a local value. In contrast, the values that are obtained in the downcomer by using videography are the quantity of gas inside a specific measuring volume. The measuring volume is composed of the cross section of the downcomer (0.06 m width and 0.05 m depth) and a height of $\Delta y=0.025$ m. The given values are placed in the middle of these volumes.

The void fraction results for the upper region of the riser and along the lower region of the downcomer are shown in Fig. 16. Measurements have been taken only in the upper region of the riser in order not to disturb the bubble plume at the bottom. From visual observation, the flow disturbance of the 0.2 mm thick probe lance in the upper region was negligible; especially the swinging

motion of the plume at the bottom was not disturbed. The void fraction inside the downcomer is determined only up to a height of 0.45 m since one of the column's flange is blocking the view. Above the flange the void fraction inside the vortex structure at the top of the internal walls, which is described above, was too high for reliable measurements with the videography method.

The void fraction inside the riser is increasing with increasing volume flow rate. Furthermore, a center peak is observed for all cases, with a maximum void fraction of around 7% for case 8.

Looking at the void fraction along the downcomer in Fig. 16, surprisingly the profiles obtained for case 6 and 8 are rather similar. The void fraction is steadily decreasing with decreasing height in general. Moreover, near the end of the internal walls (the bottom edge of the internal walls is at $y = 0.06$ m) the void fraction is rapidly decreasing due to an increasing liquid velocity at this point. The rising bubbles in the riser pull the liquid from the downcomer into the riser and, therefore, also the bubbles from the downcomer.

The general trend of a steadily decreasing void fraction along the downcomer is explained by the liquid velocity field. As a strong downward flow at the reactor wall is observed, a positive horizontal liquid velocity in the downcomer towards the internal walls occurs, as shown in Fig. 17a. Naturally, this horizontal velocity is decreasing along the downcomer, but surprisingly in the bottom region the strongest horizontal velocity is seen for case 4 whereas it is for case 8 almost zero. This behavior might be due

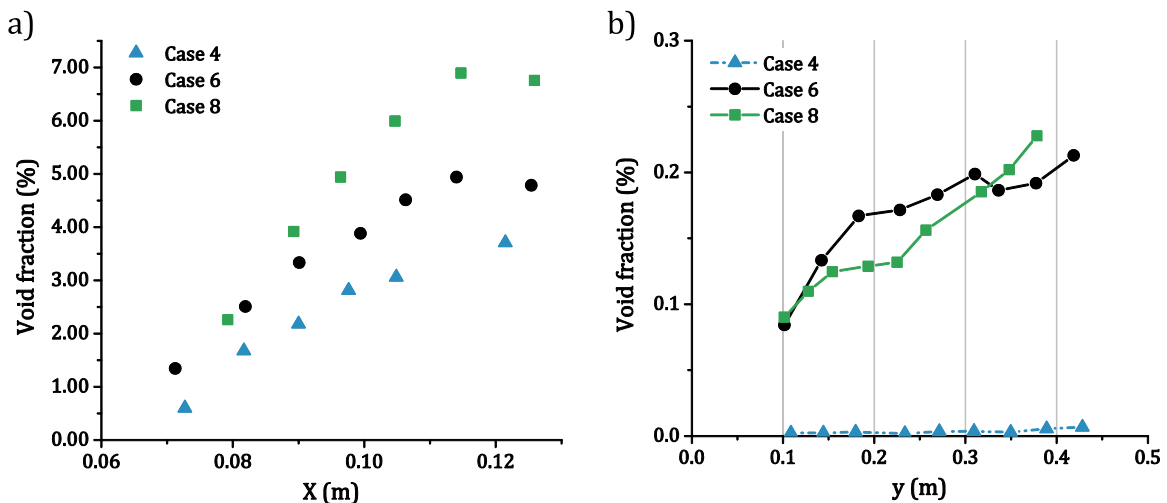


Fig. 16. Void fraction profiles in the airlift reactor. (a) In the riser at $y=0.6$ m, and (b) along the downcomer.

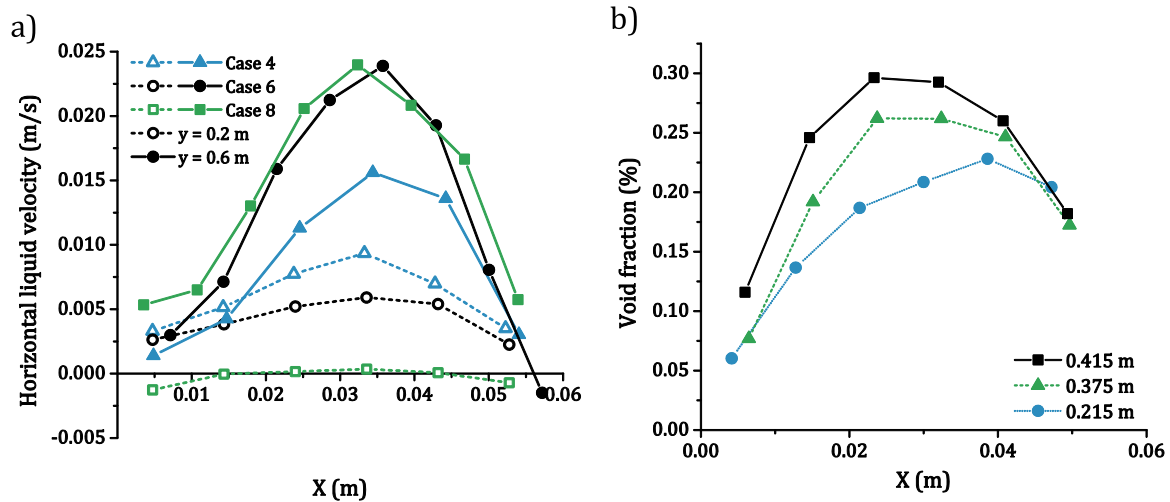


Fig. 17. Flow situation in the downcomer. (a) Horizontal liquid velocity at two different heights, and (b) void fraction profiles for case 6 at three different heights.

to the higher void fraction and/or larger bubble sizes for case 8, which lead to a higher momentum dispersion. Nevertheless, a liquid velocity that pushes the bubbles towards the internal walls is observed in the downcomer in general.

Since the bubbles are pulled into the downcomer near the reactor wall, the void fraction profile in the upper part of the downcomer at $y=0.415$ m has a peak near the reactor walls at $x=0.02$ m, as shown in Fig. 17b. Below this measuring position at $y=0.375$ m the void fraction near the reactor wall is distinctly smaller but towards the internal walls almost the same. This indicates a migration of the bubbles away from the reactor wall to the internal walls where a lower downward liquid velocity is observed so that the bubbles rise up (see Fig. 10). Nevertheless, the peak is still near $x=0.02$ m. Looking at the void fraction profile further downstream at $y=0.215$ m the maximum gas fraction is seen near the internal walls at $x=0.04$ m. Thus, more and more bubbles had moved to the internal walls.

The described transportation of the bubbles towards the internal walls in the downcomer where the bubbles can rise up leads to a steadily decreasing gas void fraction. However, in contrast to case 6 and 8 the volume fraction for case 4 in the downcomer is nearly zero. This very small void fraction inside the downcomer for case 4 is not trivial because the vertical velocity inside the downcomer is very similar compared to case 6 and case 8 (see Fig. 10). From visual observations, it was noted that only few bubbles for case 4 are dragged towards the large vortex zone in the upper region of the downcomer. This might be caused by a smaller void fraction near the internal walls in the upper region of the riser for case 4. Thus, the distribution of the bubbles at the top of the riser might determine whether bubbles are dragged to the downcomer or not.

5. Discussion and conclusion

The hydrodynamics of an airlift reactor have been investigated in order to provide data for CFD model validation. The locally resolved bubble size distribution, liquid velocity, Reynolds stresses and void fraction at different positions for three different volume flow rates have been given for this purpose. The different flow rates have been generated by changing the number of sparger needles so that the bubble size distribution is held constant. Moreover, the sum of the two downcomer flow cross sections was equal to the cross section of the riser.

The present study is situated in the regime of a constant

velocity in the downcomer as described e.g. by van Benthum, et al. (1999) or Law et al. (2013). Indeed, for case 6 and case 8 the mean velocity in the downcomer is in the range of 0.2 m/s, however, for case 4 the mean velocity is around 0.18 m/s. Therefore, case 4 might be at the beginning of this regime.

Although similar velocity profiles were obtained for the different flow rates, distinct differences have been found for the normal and cross components of the Reynolds stress tensor, especially in the riser. The turbulence parameters might contain both larger scale structures induced by the swinging bubble plume and bubble induced turbulence phenomena. In the bottom part of the riser, the large structures might be dominating whereas in the upper part the flow is homogenized so that the large structures are vanishing. Thus, a model will be needed that is able to capture such effects on all scales.

For all used sparger setups a distinct bubble plume is build up at the bottom of the riser. The circulating flow constricts the bubbles at the bottom and intensifies this effect. Because of the swinging bubble plume, the liquid velocity in the downcomer is also periodically increasing and decreasing. This effect leads also to a periodically swelling and subsiding of the void fraction inside the downcomer. However, also the situation that the bubble plume stands at one side for a longer period was observed. This situation was alternating randomly with a constant swinging bubble plume.

A large vortex structure is seen at the top of the downcomer so that bubbles are pulled into the downcomer at the reactor wall. Due to a horizontal liquid velocity, these bubbles move to the internal wall where they can rise up because the vertical velocity is smaller there. This effect leads to a steady decrease of the void fraction along the downcomer. Since the absolute velocity of the bubbles is small in the downcomer, lateral bubble forces like lift force or turbulent dispersion force might be significant in this context. The holdup in the downcomer seems to display complex behavior since for the smallest volume flow rate the void fraction is almost zero whereas for the other two the void fraction is almost similar, although the velocity is almost equal for all cases.

The complexity of the present experiments is intentional reduced by using gas volume flow rates and a sparger with which break-up and coalescence processes can be neglected. In combination with the constant bubble size distribution for all flow rates, a model validation focused on the same problem for different superficial velocities is possible. In addition, the water is reliable pure by using the naturally occurring micro bubbles as tracer for particle tracking instead of additional tracer particles. Indeed, the CFD-grade measurements are realized in general with relatively

simple methods, which might encourage other work to perform such measurements in bench-scale/small-pilot facilities since they are vitally needed.

Acknowledgment

This work was funded by the Helmholtz Association within the frame of the Helmholtz Energy Alliance “Energy Efficient Chemical Multiphase Processes” (HA-E-0004).

References

- Bozzano, G., Dente, M., 2001. Shape and terminal velocity of single bubble motion: a novel approach. *Comput. Chem. Eng.* 25, 571–576.
- Broeder, D., Sommerfeld, M., 2007. Planar shadow image velocimetry for the analysis of the hydrodynamics in bubbly flows. *Meas. Sci. Technol.* 18 (8), 2513–2528.
- Canny, J., 1986. Computational approach to edge detection. *IEEE Trans. Pattern Anal. Mach. Intell.* 8 (6), 679–698.
- Da Silva, M., Schleicher, E., Hampel, U., 2007. A novel needle probe based on high-speed complex permittivity measurements for investigation of dynamic fluid flows. *IEEE Trans. Instrum. Meas.* 56 (4), 1249–1256.
- Fernandes, B.D., Dragone, G.M., Teixeira, J.A., Vicente, A.A., 2010. Light regime characterization in an airlift photobioreactor for production of microalgae with high starch content. *Appl. Biochem. Biotechnol.*, 218–226.
- Ghasemi, H., Hosseini, S.H., 2012. Investigation of hydrodynamics and transition regime in an internal loop airlift reactor using CFD. *Braz. J. Chem. Eng.* 29, 821–833.
- Honkanen, M., Saarenrinne, P., Stoor, T., Niinimäki, J., 2005. Recognition of highly overlapping ellipse-like bubble images. *Meas. Sci. Technol.* 16 (9), 1760.
- Huang, Q., Yang, C., Yu, G., Mao, Z.-S., 2010. CFD simulation of hydrodynamics and mass transfer in an internal airlift loop reactor using a steady two-fluid model. *Chem. Eng. Sci.* 65 (20), 5527–5536.
- Ishii, M., Hibiki, T., 2006. *Thermo-fluid Dynamics of Two-phase Flow*, 2nd ed. Springer Science+Business Media, Inc., New York.
- Korpajarvi, J., Oinas, P., Reunanen, J., 1999. Hydrodynamics and mass transfer in an airlift reactor. *Chem. Eng. Sci.* 54, 2255–2262.
- Kracht, W., Emery, X., Paredes, C., 2013. A stochastic approach for measuring bubble size distribution via image analysis. *Int. J. Miner. Process.* 121, 6–11.
- Law, D., Battaglia, F., 2013. Numerical simulations for hydrodynamics of air-water external loop airlift reactor flows with bubble break-up and coalescence effects. *J. Fluids Eng.* 135, pp. 081302-1–081302-8.
- Le Corre, J.-M., Hervieu, E., Ishii, M., Delhay, J.-M., 2003. Benchmarking and improvements of measurement techniques for local-time-averaged two-phase flow parameters. *Exp. Fluids* 35 (5), 448–458.
- Liu, Y., Tay, J.-H., 2002. The essential role of hydrodynamic shear force in the formation of biofilm and granular sludge. *Water Res.* (1653–1665)
- Lu, X., Ding, J., Wang, Y., Shi, J., 2000. Comparison of the hydrodynamics and mass transfer characteristics of a modified square airlift reactor with common airlift reactors. *Chem. Eng. Sci.* 55, 2257–2263.
- Lucas, D., et al., 2016. A strategy for the qualification of multi-fluid for reactor safety. *Nucl. Eng. Des.* 299, 2–11.
- Luo, H.-P., Al-Dahhan, M.H., 2011. Verification and validation of CFD simulations for local flow dynamics in a draft tube airlift bioreactors. *Chem. Eng. Sci.* 66 (5), 907–923.
- Manera, A., et al., 2009. Comparison between wire-mesh sensors and conductive needle-probes for measurements of two-phase flow parameters. *Nucl. Eng. Des.* 239 (9), 1718–1724.
- Miron, A.S., et al., 2000. Bubble-column and airlift photobioreactors for algal culture. *AIChE J.* 49 (9), 1872–1887.
- Mudde, R.F., Lee, D.J., Reese, J., Fan, L.-S., 1997. Role of coherent structures on Reynolds stresses in a 2-D bubble column. *Part Technol. Fluid.* 43, 4.
- Oliver-Salvador, M. d C., et al., 2013. Shear rate and microturbulence effects on the synthesis of proteases by *Jacaratia mexicana* cells cultured in a bubble column, airlift, and stirred tank bioreactors. *Biotechnol. Bioprocess Eng.*, 808–818.
- Schleicher, E., Da Silva, M., Hampel, U., 2008. Enhanced local void and temperature measurements for highly transient multiphase flows. *IEEE Trans. Instrum. Meas.* 57 (2), 401–405.
- Simcik, M., 2011. CFD simulation and experimental measurement of gas hold up and liquid interstitial velocity in internal loop air lift reactor. *Chem. Eng.* 66, 3268–3279.
- Simiano, M., et al., 2006. Comprehensive experimental investigation of the hydrodynamics of large-scale, 3D, oscillating bubble plumes. *Int. J. Multiph. Flow.* 32, 1160–1181.
- van Benthum, W., van der Lans, R., van Loosdrecht, M., Heijnen, J., 1999. Bubble recirculation regimes in an internal-loop airlift reactor. *Chem. Eng. Sci.* 54 (18), 3995–4006.
- Ziegenhein, T., Lucas, D., 2016. On sampling bias in multiphase flows: particle image velocimetry in bubbly flows. *Flow Meas. Instrum.* 48, 36–41.
- Ziegenhein, T., Rzehak, R., Lucas, D., 2015. Transient simulation for large scale flow in bubble columns. *Chem. Eng. Sci.* 122 (0), 1–13.
- Ziegenhein, T., Garcon, M., Lucas, D., 2016. Particle tracking using micro bubbles. *Chem. Eng. Sci.*, (under review).